

# Density waves in the shearing sheet

## V. Feedback cycle for swing amplification by non-linear effects

B. Fuchs, C. Dettbarn, and T. Tsuchiya\*

Astronomisches Rechen-Institut am Zentrum für Astronomie der Universität Heidelberg, Mönchhofstrasse 12–14,  
69120 Heidelberg, Germany

Received 2005; accepted 2005

**Abstract.** Non-linear effects in the dynamical evolution of a shearing sheet made of stars are studied. First the implications of hitherto neglected non-linearities of the Boltzmann equation for the dynamical evolution of the shearing sheet are investigated. Using a formalism developed previously on the basis of the linearized Boltzmann equation it is demonstrated that the inclusion of the non-linear term leads to a feedback cycle for swing amplified density waves in the unbounded shearing sheet. Such a feedback is unique to star disks and is not known for gas disks. In order to present concrete examples of the non-linear feedback cycle a SCF code was developed and numerical simulations of the dynamical evolution of the shearing sheet are performed. The numerical results seem to confirm the theoretical predictions. The evolution of the shearing sheet resembles closely and might actually explain the recurrent spiral instabilities found in large-scale numerical simulations of the dynamical evolution of galactic disks.

**Key words.** galaxies: kinematics and dynamics – galaxies: spiral

### 1. Introduction

The shearing sheet (Goldreich & Lynden-Bell 1965, Julian & Toomre 1966) model has been developed as a tool to study the dynamics of galactic disks and is particularly well suited to theoretically describe the dynamical mechanisms responsible for the formation of spiral arms. For simplicity, the model describes only the dynamics of a patch of a galactic disk. It is assumed to be infinitesimally thin and its radial size is assumed to be much smaller than the disk. Polar coordinates can be therefore converted to pseudo-Cartesian coordinates and the velocity field of the differential rotation of the disk can be approximated by a linear shear flow. These simplifications allow an analytical treatment of the problem, which helps to clarify the underlying physical processes operating in the disk. In the previous papers of this series (Fuchs 2001a, b, 2004, 2005) we have studied various aspects of the dynamics of spiral density waves in a shearing sheet of stars based on the *linearized* Boltzmann equation. In the present paper we study *non-linear* effects in the dynamical evolution of the shearing sheet. In particular, we investigate the role of the hith-

erto neglected non-linear term of the Boltzmann equation. The principal result is that the non-linearity leads to a feedback cycle for swing amplification of spiral density waves. Recurrent spiral instabilities, which lead to an ever changing appearance of the disk, have been reported by Sellwood & Carlberg (1984) and Sellwood (1989) from their numerical simulations of the dynamical evolution of self gravitating, differentially rotating disks. Toomre (1990) and Toomre & Kalnajs (1991) have argued that these recurrent spiral density waves are essentially due to swing amplified (Toomre 1981) random fluctuations of the surface density of the disks. Sellwood (1989), on the other hand, points out that contrary to expectation the spiral instabilities stay at the same level of activity in the experiments, if the particle number is increased and thus the particle noise is reduced. Moreover, Sellwood & Carlberg (1984) have shown that, once the cycles of recurrent transient spiral density waves have established themselves in their simulations, the leading density wavelets which are then swing amplified are extremely unlikely due to chance alignments of the stars, because the amplitudes of these leading wavelets are too large. They consider the recurrent spirals not to be unconnected random events arising from swing amplified random noise. Sellwood (2000) puts forward the notion of a feedback mechanism for spi-

\* Present address: SGI Japan Ltd., Ebisu Garden Place Tower 31F, 4-20-3 Ebisu, Shibuya-ku, Tokyo 150-6031, Japan  
Correspondence to: fuchs@ari.uni-heidelberg.de

ral instabilities, which is related to fine structure of the distribution function of stars in phase space carved in by transient spiral density waves, which can then in turn incite density waves again. As a concrete example Sellwood & Lin (1989) and Sellwood & Kahn (1991) have developed the concept of recurring groove instabilities. These rely on fairly sharp boundaries of the dynamically active parts of the self gravitating disks, because they are initiated by edge modes (Toomre 1981). The groove instabilities develop then as rigidly rotating spiral modes of the disk<sup>1</sup> and seed fresh grooves through particle wave resonance at their Lindblad resonances. However, Sellwood & Carlberg (1984) have shown in detail that the spiral structures seen in their numerical simulations are transient swing amplified shearing density waves exactly of the kind found in the infinite shearing sheet model. They demonstrate not only that the spiral arms shear from leading to trailing orientation, but also that the density waves grow preferentially with azimuthal wave numbers predicted by the shearing sheet model, which has become widely known as the Toomre (1981) “ $X = 2$ ” prescription. Exactly the same was found by Fuchs & von Linden (1998) in their numerical simulations of the dynamical evolution of a self gravitating disk made of stars and interstellar gas. Toomre (1990) has argued convincingly that the spiral arms of Sc galaxies are such transient shearing density waves. One of the deeper reasons for this success of the infinite shearing sheet model in describing spiral density waves realistically is the rapid convergence of the Poisson integral in self gravitating disks (Julian & Toomre 1966). Consider, for example, the potential of a sinusoidal density perturbation

$$\Phi(x, y) = -G \int_{-\infty}^{\infty} dx' \int_{-\infty}^{\infty} dy' \frac{\Sigma_{10} \sin(kx')}{\sqrt{(x-x')^2 + (y-y')^2}}, \quad (1)$$

where  $G$  denotes the constant of gravitation. At  $y = 0$

$$\Phi = -4G\Sigma_{10} \sin(kx) \lim_{x_L \rightarrow \infty} \frac{\text{Si}(kx_L)}{k} = -\frac{2\pi G\Sigma_{10} \sin(kx)}{k}. \quad (2)$$

The sine integral in equation (2) converges so rapidly that at  $kx_L = \frac{\pi}{2}$  it reaches already 87% of its asymptotic value. Thus the “effective range” of gravity is only about a quarter of a wave length. The shearing sheet models effectively patches of galactic disks of such size. Thus the shearing sheet model seems to be a well suited tool to interpret the recurring transient spiral instabilities seen in the numerical simulations of self gravitating disks. Of course, the shearing sheet model with its rather drastic simplifications such as the neglected curvature of the mean guiding centers of the stellar orbits and the assumed homogeneous mass distribution or the periodic boundary conditions in

numerical simulations of the dynamical evolution has its limitations. Sellwood & Carlberg (1984) noted in particular that the maximum growth factors of the shearing density waves in their simulations are somewhat larger than the predictions of the local model. Similarly Toomre (1981) finds also greater amplification of density waves in the full disk model of Zang.

It is the aim of the present paper to demonstrate on the basis of the infinite shearing sheet model that a feedback cycle of swing amplified density waves is indeed theoretically expected. In the next section a formal derivation is presented, while in the third section we describe numerical SCF simulations of the dynamical evolution of the shearing sheet and illustrate the feedback cycle with concrete examples. The SCF simulations are directly compared with N-body simulations of the dynamical evolution of the shearing sheet by Toomre (1990), Toomre & Kalnajs (1991) and Chiueh & Tseng (2000).

Non-linear interaction of density waves has been previously studied by Tagger et al. (1987) and Sygnet et al. (1988). These authors considered, however, the interaction of rigidly rotating, slowly growing spiral modes, which do not develop in the unbounded shearing sheet. A preliminary report on the work presented here was given in Fuchs (1991).

## 2. Theoretical considerations

### 2.1. Boltzmann equation

The time evolution of the distribution function of stars in phase space,  $f$ , is determined by the collisionless Boltzmann equation

$$\frac{\partial f}{\partial t} + [f, H] = 0, \quad (3)$$

where the square bracket indicates the usual Poisson bracket and  $H$  is the Hamiltonian of the stellar orbits (cf. paper I). Spiral arms are usually thought to be only minor perturbations of galactic disks. Thus we choose as in the previous studies a perturbation ‘Ansatz’ of the form

$$f = f_0 + \delta f, \quad H = H_0 + \delta\Phi, \quad (4)$$

where  $f_0$  and  $H_0$  refer to the unperturbed shearing sheet, respectively. The physical idea is to subject the shearing sheet to a small spiral-like potential perturbation  $\delta\Phi$  and to determine the disk response  $\delta f$  by solving the Boltzmann equation. Inserting the ‘Ansatz’ (4) into the Boltzmann equation (3) leads to

$$\frac{\partial \delta f}{\partial t} + [f_0, \delta\Phi] + [\delta f, H_0] = -[\delta f, \delta\Phi], \quad (5)$$

where the rhs represents the non-linear term of the Boltzmann equation. The background distribution function  $f_0$  is chosen in the following, again in the form of a Schwarzschild distribution function.

<sup>1</sup> It can be shown (Toomre & Kalnajs 1980, unpublished results, Sellwood & Kahn 1991, Fuchs 2005) that even the shearing sheet develops rigidly propagating, exponentially growing spiral modes, if a sharp left hand boundary is introduced.

The non-linear Poisson bracket has the explicit form

$$[\delta f, \delta \Phi] = \frac{\partial \delta f}{\partial w_1} \frac{\partial \delta \Phi}{\partial J_1} + \frac{\partial \delta f}{\partial w_2} \frac{\partial \delta \Phi}{\partial J_2} - \frac{\partial \delta f}{\partial J_1} \frac{\partial \delta \Phi}{\partial w_1} - \frac{\partial \delta f}{\partial J_2} \frac{\partial \delta \Phi}{\partial w_2}, \quad (6)$$

if we use again the variables introduced in paper (I).  $J_1$  denotes the radial action integral of a stellar orbit and  $J_2$  is an integral of motion related to angular momentum.  $w_1$  and  $w_2$  are the canonical conjugate variables, respectively. In expression (6) the perturbation of the distribution function can be Fourier analyzed as

$$\delta f = \sum_{l_1} \int dl_2 f_1(\mathbf{J}) e^{i[l_1 w_1 + l_2 w_2]}. \quad (7)$$

Since  $w_1$  is a genuine angle variable,  $l_1$  denotes integer numbers, whereas  $l_2$  is a real variable. The perturbation of the gravitational potential is Fourier analyzed as

$$\delta \Phi = \int dk_x \int dk_y \Phi_{\mathbf{k}} e^{i[k_x x + k_y y]} \quad (8)$$

where  $x$  and  $y$  denote the pseudo-Cartesian spatial coordinates of the shearing sheet with  $y$  pointing in the direction of rotation. Using the orbit equations derived in paper (I) the Fourier expansion in equation (8) takes the form

$$\exp i[k_x x + k_y y] = \exp i \left( k_x \frac{J_2 - \Omega_0}{-2B} + k_x \sqrt{\frac{2J_1}{\kappa}} \sin w_1 + k_y w_2 - k_y \frac{\sqrt{2\kappa J_1}}{2B} \cos w_1 \right) \quad (9)$$

with Oort's second constant  $B$  and the epicyclic frequency  $\kappa$ . We refer to paper (I) for the meaning of  $\Omega_0$  and  $r_0$ , which define the center of the shearing sheet. Inserting the two Fourier components from equations (7) and (8) into the non-linear Poisson bracket (6) leads to

$$\begin{aligned} [\delta f, \delta \Phi] = & \left( -l_1 \frac{\xi}{2J_1} \sin(w_1 - \bar{w}) f_1 - l_2 \frac{k_x}{-2B} f_1 \right. \\ & \left. - i k_y \frac{\partial f_1}{\partial J_2} - i \frac{\partial f_1}{\partial J_1} \xi \cos(w_1 - \bar{w}) \right) \Phi_{\mathbf{k}} \\ & \times \exp i \left( l_1 w_1 + l_2 w_2 + k_x \frac{J_2 - \Omega_0 r_0}{-2B} \right. \\ & \left. + k_y w_2 + \xi \sin(w_1 - \bar{w}) \right), \end{aligned} \quad (10)$$

where the auxiliary variables  $\xi$  and  $\bar{w}$  are defined as in paper (I) as  $\xi = \sqrt{\frac{2J_1}{\kappa}} \sqrt{k_x^2 + \frac{\kappa^2}{4B^2} k_y^2}$  and  $\bar{w} = \arctan(\frac{\kappa}{2B} \frac{k_y}{k_x})$ , respectively.

## 2.2. Solution of the Boltzmann equation

The Boltzmann equation (5) can be viewed as a linear partial differential equation for  $\delta f$  with the two inhomogeneous terms  $[f_0, \delta \Phi]$  and  $[\delta f, \delta \Phi]$ , respectively. Formally it can be solved for each inhomogeneity separately and both solutions can be then combined as the final solution

$$\delta f = \delta f_1 + \delta f_2. \quad (11)$$

The linearized Boltzmann equation

$$\frac{\partial \delta f_1}{\partial t} + [\delta f_1, H_0] = -[f_0, \delta \Phi] \quad (12)$$

has already been solved in paper (I) and we can use directly the result obtained there. This leaves the second equation

$$\frac{\partial \delta f_2}{\partial t} + [\delta f_2, H_0] = -[\delta f, \delta \Phi] \quad (13)$$

to be treated here, which takes the explicit form

$$\begin{aligned} \frac{\partial \delta f_2}{\partial t} + \kappa \frac{\partial \delta f_2}{\partial w_1} + \frac{A}{B} (J_2 - \Omega_0 r_0) \frac{\partial \delta f_2}{\partial w_2} = & \left( l_1 \frac{\xi}{2J_1} \sin(w_1 - \bar{w}) f_1 + l_2 \frac{k_x}{-2B} f_1 \right. \\ & \left. + i k_y \frac{\partial f_1}{\partial J_2} + i \frac{\partial f_1}{\partial J_1} \xi \cos(w_1 - \bar{w}) \right) \Phi_{\mathbf{k}} \\ & \times \exp i \left( l_1 w_1 + l_2 w_2 + k_x \frac{J_2 - \Omega_0 r_0}{-2B} \right. \\ & \left. + k_y w_2 + \xi \sin(w_1 - \bar{w}) \right) \end{aligned} \quad (14)$$

with the first Oort constant  $A = \Omega_0 + B$ . Equation (14) is of the same form as equation (20) of paper (I) and can be treated in the same way. Since the coefficients of the differential equation (14) do not depend on time  $t$  or the variable  $w_2$ , equation (14) can be Fourier transformed with respect to  $t$  and  $w_2$  leading to

$$\begin{aligned} i\omega f_{2,\omega} + \kappa \frac{df_{2,\omega}}{dw_1} + i(k_y + l_2) \frac{A}{B} (J_2 - \Omega_0 r_0) f_{2,\omega} = & \left( l_1 \frac{\xi}{2J_1} \sin(w_1 - \bar{w}) f_1 \Phi_{\mathbf{k}}|_{\omega} + l_2 \frac{k_x}{-2B} f_1 \Phi_{\mathbf{k}}|_{\omega} \right. \\ & \left. + i k_y \frac{\partial f_1}{\partial J_2} \Phi_{\mathbf{k}}|_{\omega} + i \frac{\partial f_1}{\partial J_1} \Phi_{\mathbf{k}}|_{\omega} \xi \cos(w_1 - \bar{w}) \right) \\ & \times \exp i \left( l_1 w_1 + l_2 w_2 + k_x \frac{J_2 - \Omega_0 r_0}{-2B} \right. \\ & \left. + k_y w_2 + \xi \sin(w_1 - \bar{w}) \right). \end{aligned} \quad (15)$$

Notice that the products of  $f_1$  and  $\Phi_{\mathbf{k}}$  and  $\frac{\partial f_1}{\partial J_{1,2}}$  and  $\Phi_{\mathbf{k}}$ , respectively, have been Fourier transformed with respect to time simultaneously, which has to be taken into account when transforming back from frequency to the time domain. Equation (15) is of exactly the same form as equation (23) of paper (I) and can be solved in the same way by determining first the solution of the homogeneous part of the equation, then constructing a particular integral of the inhomogeneous equation by 'variation of the constant', and finally adjusting the constant of integration so that the solution is uniquely defined in velocity space. We report here only the final result

$$\begin{aligned} f_{2,\omega} = & \frac{e^{i[\pi\eta + l_1 w_1]}}{2i \sin \pi\eta} \exp i[\omega t + (k_y + l_2)w_2 + k_x \frac{J_2 - \Omega_0 r_0}{-2B}] \\ & \times \left[ \left( \frac{1}{-2B} l_2 k_x f_1 \Phi_{\mathbf{k}}|_{\omega} + i k_y \frac{\partial f_1}{\partial J_2} \Phi_{\mathbf{k}}|_{\omega} \right) \right. \\ & \left. \times \int_{-\pi}^0 dw'_1 \exp i[(l_1 + \eta)w'_1 + \xi \sin(w'_1 + w_1 - \bar{w})] \right] \end{aligned}$$

$$\begin{aligned}
& + l_1 \frac{\xi}{2J_1} f_1 \Phi_{\mathbf{k}}|_{\omega} \int_{-2\pi}^0 dw'_1 \sin(w'_1 + w_1 - \bar{w}) \\
& \times \exp i[(l_1 + \eta)w'_1 + \xi \sin(w'_1 + w_1 - \bar{w})] \\
& + i\xi \frac{\partial f_1}{\partial J_1} \Phi_{\mathbf{k}}|_{\omega} \int_{-2\pi}^0 dw'_1 \cos(w'_1 + w_1 - \bar{w}) \\
& \times \exp i[(l_1 + \eta)w'_1 + \xi \sin(w'_1 + w_1 - \bar{w})] \Big], \quad (16)
\end{aligned}$$

where  $\eta = \frac{1}{\kappa} \left( \omega + (k_y + l_2) \frac{A}{B} (J_2 - \Omega_0 r_0) \right)$  has been introduced as an abbreviation to keep the formulae a little more compact.  $w'_1$  is an auxiliary variable.

### 2.3. Self consistent perturbations

Even in the linear case the spatial pattern of the disk response is different to that of the imprinted potential perturbation (cf. equations 10 of paper I). In particular, through the dependence on  $\eta$  and thus on the  $J_2$  variable there is a further dependence of the disk response on the  $x$  coordinate. This means that the disk response to a Fourier component of the potential is *not* a Fourier component of the general disk response. Kalnajs (1971) has shown a way to overcome this difficulty by integrating the disk response over all wave numbers and then Fourier transforming this with respect to the spatial  $x$  and  $y$  coordinates again. The result is integrated over velocity space in order to obtain the surface density of the disk response and inserted into the Poisson equation whose lhs is also Fourier transformed,

$$\begin{aligned}
& \frac{1}{(2\pi)^2} \int_{-\infty}^{+\infty} dz \int_{-\infty}^{+\infty} dx \int_{-\infty}^{+\infty} dy e^{-i[k'_x x + k'_y y]} \\
& \left\{ \frac{\partial^2}{\partial x^2} + \frac{\partial^2}{\partial y^2} + \frac{\partial^2}{\partial z^2} \right\} \int_{-\infty}^{+\infty} dk_x \int_{-\infty}^{+\infty} dk_y \Phi_{\mathbf{k}}|_{\omega} \\
& \times \exp \left[ i[k'_x x + k'_y y] - \sqrt{k_x'^2 + k_y'^2} |z| \right] \\
& = -2\sqrt{k_x'^2 + k_y'^2} \Phi_{\mathbf{k}}|_{\omega} e^{i[k'_x x + k'_y y]} \\
& = \frac{4\pi G}{(2\pi)^2} \int_{-\infty}^{+\infty} dx \int_{-\infty}^{+\infty} dy e^{-i[k'_x x + k'_y y]} \\
& \int_{-\infty}^{+\infty} dk_x \int_{-\infty}^{+\infty} dk_y \int_{-\infty}^{+\infty} du \int_{-\infty}^{+\infty} dv \delta f. \quad (17)
\end{aligned}$$

In this way self consistent perturbations of a self gravitating disk can be calculated (cf. equations 35 and 36 of paper I). Accordingly, on the rhs of equation (17) a multiple integral over the disk response to the non-linear term of the form

$$\begin{aligned}
& \frac{4\pi G}{(2\pi)^2} \int_0^{+\infty} dJ_1 \int_{-\infty}^{+\infty} dJ_2 \int_0^{2\pi} dw_1 \int_{-\infty}^{+\infty} dw_2 \\
& \sum_{l_1=-\infty}^{\infty} \int_{-\infty}^{+\infty} dl_2 \int_{-\infty}^{+\infty} dk_x \int_{-\infty}^{+\infty} dk_y \\
& \exp -i \left[ k'_x \frac{J_2 - \Omega_0 r_0}{-2B} + k'_y w_2 + \xi' \sin(w_1 - \bar{w}') \right]
\end{aligned}$$

$$\begin{aligned}
& \times \frac{e^{i[\pi\eta + l_1 w_1]}}{2i \sin \pi\eta} \exp i[\omega t + (k_y + l_2)w_2 + k_x \frac{J_2 - \Omega_0 r_0}{-2B}] \\
& \times \left[ \left( \frac{1}{-2B} l_2 k_x f_1 \Phi_{\mathbf{k}}|_{\omega} + i k_y \frac{\partial f_1}{\partial J_2} \Phi_{\mathbf{k}}|_{\omega} \right) \right. \\
& \times \int_{-2\pi}^0 dw'_1 \exp i[(l_1 + \eta)w'_1 + \xi \sin(w'_1 + w_1 - \bar{w})] \\
& + l_1 \frac{\xi}{2J_1} f_1 \Phi_{\mathbf{k}}|_{\omega} \int_{-2\pi}^0 dw'_1 \sin(w'_1 + w_1 - \bar{w}) \\
& \times \exp i[(l_1 + \eta)w'_1 + \xi \sin(w'_1 + w_1 - \bar{w})] \\
& + i\xi \frac{\partial f_1}{\partial J_1} \Phi_{\mathbf{k}}|_{\omega} \int_{-2\pi}^0 dw'_1 \cos(w'_1 + w_1 - \bar{w}) \\
& \left. \times \exp i[(l_1 + \eta)w'_1 + \xi \sin(w'_1 + w_1 - \bar{w})] \right]. \quad (18)
\end{aligned}$$

has to be considered. Again we have changed from spatial  $(x, y)$  and  $(u, v)$  velocity coordinates to  $(J_1, J_2)$  and  $(w_1, w_2)$  coordinates.  $\xi'$  and  $\bar{w}'$  are defined in an analogous way to  $\xi$  and  $\bar{w}$ , respectively, for primed wave numbers. The integrations with respect to  $J_1$  and  $J_2$  cannot be carried out directly, because  $f_1(\mathbf{J})$  is not known explicitly. Integrations over the angle variables  $w_1$  and  $w'_1$  lead to intermediate results which are not enlightening. But the integration over the  $w_2$  variable gives immediately

$$\frac{1}{2\pi} \int_{-\infty}^{+\infty} dw_2 e^{i[k_y + l_2 - k'_y]w_2} = \delta(k_y + l_2 - k'_y). \quad (19)$$

The integration over the wave number  $k_y$  contracts the integrand of (18) to  $k_y = k'_y - l_2$ , which is the customary sum rule of wave numbers well known from plasma physics. There is an analogous sum rule for the  $k_x$  wave numbers, which is, however, not directly obvious from expression (18) because of the different Fourier transforms in equations (7) and (8).

### 2.4. Volterra integral equation

It was shown in paper (I) that the solution of the linearized Boltzmann equation (12) leads, upon inserting it into the Fourier transformed Poisson equation (17), to the Volterra integral equation ( $k'_y > 0$ )

$$\Phi_{\mathbf{k}'} = \int_{-\infty}^{k'_x} dk_x \mathcal{K}(k_x, k'_x) \Phi_{\mathbf{k}} + r_{\mathbf{k}'}^l, \quad (20)$$

where the kernel  $\mathcal{K}$  is given by equation (67) of paper (I).  $r_{\mathbf{k}'}^l$  describes an inhomogeneity of equation (20) related either to an initial non-equilibrium state of the shearing sheet or an external perturbation. The formal solution of equation (13) as derived in the previous section and then inserted into the Fourier transformed Poisson equation (17) has to be added to the rhs of equation (20) in order to obtain the solution of the non-linear Boltzmann equation. This means formally a further inhomogeneity of the Volterra equation (20),  $r_{\mathbf{k}'}^{nl}$ , which is given by (cf. equation 36 of paper I)

$$r_{\mathbf{k}'}^{nl} = \frac{2G}{-2\sqrt{k_x'^2 + k_y'^2}} \int_0^{+\infty} dJ_1 \int_{-\infty}^{+\infty} dJ_2 \int_0^{2\pi} dw_1$$

$$\begin{aligned}
& \sum_{l_1=-\infty}^{\infty} \int_{-\infty}^{+\infty} dl_2 \int_{-\infty}^{+\infty} dk_x \\
& \exp -i \left[ k'_x \frac{J_2 - \Omega_0 r_0}{-2B} + \xi' \sin(w_1 - \overline{w'}) \right] \\
& \times \frac{e^{i[\pi\eta + l_1 w_1]}}{2i \sin \pi\eta} \exp i \left[ \omega t + k'_y w_2 + k_x \frac{J_2 - \Omega_0 r_0}{-2B} \right] \\
& \times \left[ \left( \frac{1}{-2B} l_2 k_x f_1 \Phi_k|_{\omega} + i k_y \frac{\partial f_1}{\partial J_2} \Phi_k|_{\omega} \right) \right. \\
& \times \int_{-2\pi}^0 dw'_1 \exp i[(l_1 + \eta)w'_1 + \xi \sin(w'_1 + w_1 - \overline{w})] \\
& + l_1 \frac{\xi}{2J_1} f_1 \Phi_k|_{\omega} \int_{-2\pi}^0 dw'_1 \sin(w'_1 + w_1 - \overline{w}) \\
& \times \exp i[(l_1 + \eta)w'_1 + \xi \sin(w'_1 + w_1 - \overline{w})] \\
& + i \xi \frac{\partial f_1}{\partial J_1} \Phi_k|_{\omega} \int_{-2\pi}^0 dw'_1 \cos(w'_1 + w_1 - \overline{w}) \\
& \left. \times \exp i[(l_1 + \eta)w'_1 + \xi \sin(w'_1 + w_1 - \overline{w})] \right]. \quad (21)
\end{aligned}$$

The Volterra equation (20) is derived in the frequency domain. If transformed back to the time domain, we find for the linear part

$$\begin{aligned}
\Phi_{\mathbf{k}'}(t) &= 2A|k'_y| \int_{-\infty}^t dt' \tilde{\mathcal{K}}(k'_x - 2Ak'_y(t-t'), k'_x) \\
&\times \Phi_{k'_x - 2Ak'_y(t-t'), k'_y}(t') + r_{\mathbf{k}'}^l(t), \quad (22)
\end{aligned}$$

where the overhead tilde indicates that the  $\omega$ -dependent term of the kernel  $\mathcal{K}$  has been split off. In deriving equation (22), use of the convolution theorem of the Fourier transform of products of functions has been made (cf. paper I). In order to transform the non-linear term back into the time domain we consider first in expression (21) the terms that depend explicitly on  $\omega$ ,

$$\begin{aligned}
& \int_{-\infty+i\nu}^{\infty+i\nu} d\omega e^{i[\omega t + \pi\eta + \eta w'_1]} \frac{1}{\sin(\pi\eta)} = \\
& \kappa \int_{-\infty+i\frac{\kappa}{\kappa}}^{\infty+i\frac{\kappa}{\kappa}} d\eta e^{i[(\kappa\eta - \frac{A}{B}(J_2 - \Omega_0 r_0)k'_y)t + \eta w'_1]} \frac{e^{i\pi\eta}}{\sin(\pi\eta)} \quad (23)
\end{aligned}$$

with  $\eta = \frac{1}{\kappa}(\omega + \frac{A}{B}(J_2 - \Omega_0 r_0)k'_y)$ . According to Landau's rule the imaginary part of the frequency is chosen negative,  $\Im(\omega) = \nu < 0$ . By deforming the integration contour in the complex frequency plane we find that expression (23) is proportional to the unit step function

$$u(\kappa t + w'_1) = \begin{cases} 1, & \kappa t + w'_1 \geq 0 \\ 0, & \kappa t + w'_1 < 0 \end{cases}. \quad (24)$$

Thus the inhomogeneity (21) of the Volterra equation can be cast formally into the form

$$\begin{aligned}
r_{\mathbf{k}'}^{nl}(t) &= 2G \int_0^{+\infty} dJ_1 \int_{-\infty}^{+\infty} dJ_2 \int_0^{2\pi} dw_1 \\
& \sum_{l_1=-\infty}^{\infty} \int_{-\infty}^{+\infty} dl_2 \int_{-\infty}^{+\infty} dk_x \int_{-2\pi}^0 dw'_1 \int_{-\infty}^{t+w'_1/\kappa} dt' \\
& \left[ \mathcal{N}_1(\mathbf{J}, w_1, w'_1, \mathbf{l}, k_x, \mathbf{k}', t-t') f_1(t') \Phi_{k_x, k'_y-l_2}(t') \right.
\end{aligned}$$

$$\begin{aligned}
& + \mathcal{N}_2(\mathbf{J}, w_1, w'_1, \mathbf{l}, k_x, \mathbf{k}', t-t') \frac{\partial f_1}{\partial J_1} \Big|_{t'} \Phi_{k_x, k'_y-l_2}(t') \\
& \left. + \mathcal{N}_3(\mathbf{J}, w_1, w'_1, \mathbf{l}, k_x, \mathbf{k}', t-t') \frac{\partial f_1}{\partial J_2} \Big|_{t'} \Phi_{k_x, k'_y-l_2}(t') \right], \quad (25)
\end{aligned}$$

which has to be added to the rhs of equation (22). Again use of the convolution theorem of the Fourier transform of products of functions has been made. Since  $w'_1$  is less than or equal to zero, the integration over time  $t'$  extends to the upper limit  $t$ .

## 2.5. Discussion of the Volterra equation

The Volterra equation (22) augmented by  $r_{\mathbf{k}'}^{nl}$  reveals clearly the role of the non-linear term of the Boltzmann equation in the dynamical evolution of the shearing sheet.

In Fig. 1 the linear evolution of a density wave, calculated neglecting the non-linear part of equation (22), is illustrated. The density wave is initialized as

$$r_{\mathbf{k}'} \propto \delta(k'_x - (k_x^{\text{in}} + 2Ak'_y t)) \delta(k'_y - k_y^{\text{in}}) e^{-\frac{t^2}{T^2}}, \quad (26)$$

where  $T$  is a time constant. As can be seen from Fig. 1 or directly from the interplay of the indices of the Fourier coefficients of the gravitational potential in the linear equation (22),  $k'_x - 2Ak'_y(t-t')$ , with time  $t'$  at which the Fourier coefficients are taken, the delta impulse travels at constant wave number  $k_y^{\text{in}}$  to positive wave numbers  $k_x$  at a speed of  $\dot{k}_x^{\text{eff}} = 2Ak_y^{\text{in}}$ . The wave crests of the density waves are oriented perpendicular to the wave vectors, which means that the wave crests swing around from leading to trailing orientation. While swinging around the wave is amplified and then dies out. In addition the amplitude shows oscillatory behaviour. Trailing density waves are not effectively amplified (cf. paper I). Since no outer boundaries have been introduced, no rigidly rotating spiral modes appear in the shearing sheet (cf. paper II). If the non-linear term is taken into account in equation (22), the evolution of the shearing sheet becomes more complicated. In the non-linear term (25) Fourier coefficients of the perturbations of the distribution function and the gravitational potential are combined. Since the non-linear term represents an inhomogeneity of the Volterra integral equation, each combination of the Fourier coefficients sampled over times  $t'$  earlier than  $t$  provides fresh input for the swing amplification mechanism. It is instructive to rewrite the inhomogeneity  $r_{\mathbf{k}'}^{nl}$  given by equation (25) formally as

$$r_{\mathbf{k}'}^{nl}(t) = \int_{-\infty}^t dt_0 \delta(t-t_0) r_{\mathbf{k}'}^{nl}(t_0) \quad (27)$$

and to consider for each  $t_0$ -epoch the corresponding Volterra equation

$$\begin{aligned}
\Phi_{\mathbf{k}', t_0}(t) &= 2A|k'_y| \int_{-\infty}^t dt' \tilde{\mathcal{K}}(k'_x - 2Ak'_y(t-t'), k'_x) \\
&\times \Phi_{k'_x - 2Ak'_y(t-t'), k'_y, t_0}(t') + \delta(t-t_0) r_{\mathbf{k}'}^{nl}(t_0). \quad (28)
\end{aligned}$$

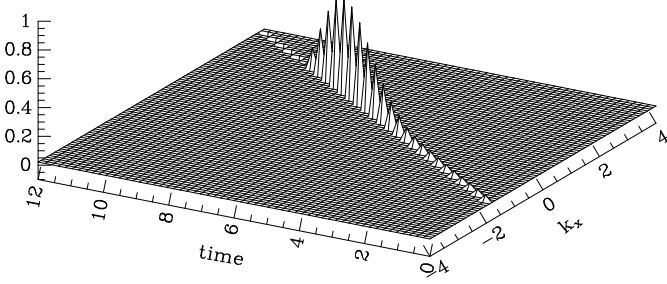


**Fig. 1.** Linear swing amplification of a density wave in the shearing sheet. The wave is initialized as a delta like impulse in wave number space with an initial wave vector  $(k_x^{\text{in}}, k_y^{\text{in}}) = (-2, 0.5) k_{\text{crit}}$ , which corresponds to initially leading arms, and an initial amplitude of 0.04. The impulse travels at constant wave number  $k_y^{\text{in}}$  with an effective radial wave number  $k_x^{\text{eff}} = k_x^{\text{in}} + 2Ak_y^{\text{in}}t$ . The wave numbers are given in units of  $k_{\text{crit}}$  defined below, and the time unit is  $\Omega_0^{-1}$ , the inverse of the mean angular velocity of the shearing sheet. Negative amplitudes at  $t > 9.5\Omega_0^{-1}$  are not shown. The parameters of the disk model are  $A/\Omega_0 = 0.5$  and  $Q = 1.4$ .

Obviously the full Volterra equation is given by the superposition

$$\begin{aligned} \Phi_{\mathbf{k}'}(t) = & \int_{-\infty}^t dt_0 \Phi_{\mathbf{k}', t_0}(t) = \\ & 2A|k_y'| \int_{-\infty}^t dt' \tilde{\mathcal{K}}(k_x' - 2Ak_y'(t-t'), k_x') \\ & \times \int_{-\infty}^t dt_0 \Phi_{\mathbf{k}_x' - 2Ak_y'(t-t'), \mathbf{k}_y', t_0}(t') + r_{\mathbf{k}'}^{\text{nl}}(t). \end{aligned} \quad (29)$$

As can be seen from equation (28) each  $\delta$ -impulse, sampling the history of the evolution of the sheet prior to  $t_0$ , is propagated linearly to time  $t$  *independently* of the following evolution of the sheet. On the other hand, these linearly evolving  $\delta$ -impulses influence later  $\delta$ -impulses by non-linear interaction of the Fourier components, always cascading off fresh input for the swing amplification mechanism. Only at  $t_0 = t$  is there an instantaneous non-linear interaction of the Fourier components. Thus the non-linear interactions lead *inter alia* to a feedback cycle for swing amplification. Even the interaction of a pair of trailing Fourier components ( $\mathbf{k} > 0$ ), which are decaying, if coupled so that their wave vectors are subtracted from each other, leads to leading density waves as an input to the swing amplification mechanism, which is then amplified accordingly. Combined with some residual particle noise this might well account for the recurrent spiral instabilities reported from the numerical simulations. As mentioned above, Sellwood & Carlberg (1984) have demonstrated by analyzing the evolution of individual spiral arms in their simulations that these are indeed swing amplified density waves of the same type as in the shearing sheet. The effect of the non-linear term of the Boltzmann equation thus has aspects that are completely different to the effects of non-linear terms in the hydrodynamical

or Jeans equations. If the latter are used to describe the dynamics of density waves, the non-linear advective and enthalpy terms imply instantaneous non-linear interaction of the Fourier components and have been shown to lead to saturation and soliton-like self-modulation effects of the density waves (Ikeuchi & Nakamura 1976, Norman 1978, Meinel 1983).

The feedback cycle described here is of course an effect depending quadratically on the magnitude of the perturbations of the sheet. Thus, if the amplitudes of the density waves are at very low levels, the efficiency of the swing amplification mechanism might not be sufficient to sustain the cycle and it will die out eventually.

### 3. Numerical self consistent field simulations

In the previous section we have developed the theoretical concept of a feedback cycle for density waves in the shearing sheet mitigated by the non-linear coupling of the waves. In order to demonstrate concrete examples of this effect we have run numerical simulations of the dynamical evolution of the shearing sheet.

#### 3.1. Self consistent field method (SCF)

The SCF method relies on a complete set of pairwise basis functions into which the density of the particles and the gravitational potential are simultaneously expanded. Each of the pairwise basis functions solve the Poisson equation. For the shearing sheet these are simply Fourier transforms,

$$\Sigma(\mathbf{R}) = \int d^2k \Sigma_{\mathbf{k}} e^{i(\mathbf{k}, \mathbf{R})}, \quad (30)$$

for the surface density of the sheet, and

$$\Phi(\mathbf{R}, z=0) = \int d^2k \Phi_{\mathbf{k}} e^{i(\mathbf{k}, \mathbf{R})} \quad (31)$$

with

$$\Phi_{\mathbf{k}} = -\frac{2\pi G}{k} \Sigma_{\mathbf{k}} \quad (32)$$

for the gravitational potential, where  $k = |\mathbf{k}|$  (cf. equations 32 to 34 of paper I). Changing to real quantities the transformation pair can be written as

$$\begin{aligned} A(\mathbf{k}) &= \int d^2R \Sigma(\mathbf{R}) \cos(\mathbf{k}, \mathbf{R}), \quad A(-\mathbf{k}) = A(\mathbf{k}), \\ B(\mathbf{k}) &= \int d^2R \Sigma(\mathbf{R}) \sin(\mathbf{k}, \mathbf{R}), \quad B(-\mathbf{k}) = -B(\mathbf{k}), \\ \Sigma(\mathbf{R}) &= \frac{1}{2\pi^2} \int_{-\infty}^{\infty} dk_x \int_0^{\infty} dk_y (A(\mathbf{k}) \cos(\mathbf{k}, \mathbf{R}) \\ &\quad + B(\mathbf{k}) \sin(\mathbf{k}, \mathbf{R})), \\ \Phi(\mathbf{R}, z=0) &= -\frac{G}{\pi} \int_{-\infty}^{\infty} dk_x \int_0^{\infty} dk_y \\ &\quad \times \frac{1}{k} (A(\mathbf{k}) \cos(\mathbf{k}, \mathbf{R}) + B(\mathbf{k}) \sin(\mathbf{k}, \mathbf{R})). \end{aligned} \quad (33)$$

**Fig. 2.** Initial set up of the 32768 particles in the simulation of the shearing sheet. The  $y$ -axis points into the direction of the shear flow. The size is  $2x_0 \times 2y_0 = 20 \times 28\lambda_{\text{crit}}$ .

In the simulation the surface density is given by

$$\Sigma(\mathbf{R}) = \sum_{j=1}^N \Delta\Sigma \delta(x - x_j) \delta(y - y_j), \quad (34)$$

where  $(x_j, y_j)$  denotes the position of particle  $j$ .  $\Delta\Sigma$  is its contribution to the surface density,  $\Delta\Sigma = \Sigma_0/N$ . Accordingly we find from equations (33)

$$\begin{aligned} A(\mathbf{k}) &= \sum_{j=1}^N \Delta\Sigma \cos(\mathbf{k}, \mathbf{R}_j) - 4\Sigma_0 \frac{\sin(k_x x_0)}{k_x} \frac{\sin(k_y y_0)}{k_y}, \\ B(\mathbf{k}) &= \sum_{j=1}^N \Delta\Sigma \sin(\mathbf{k}, \mathbf{R}_j). \end{aligned} \quad (35)$$

In practice we cannot simulate an infinite sheet, but choose a finite size  $2x_0 \times 2y_0$ . This active sheet is surrounded by virtual sheets of the same size sliding along the central sheet according to the linear shear flow. If particles are leaving the active sheet across one side, they are re-fed into the opposite side as if entering from one of the neighbouring virtual sheets with exactly the same particle distribution as in the active sheet (Wisdom & Tremaine 1988, Toomre 1990). Moreover, the SCF method is meant to simulate the fluctuations of the surface density of the sheet. Thus we have subtracted in equations (35) the Fourier coefficients of the unperturbed background density  $\Sigma_0$

$$\begin{aligned} &\int_{-x_0}^{x_0} dx \int_{-y_0}^{y_0} dy \Sigma_0 e^{-i(\mathbf{k}, \mathbf{R})} = \\ &4\Sigma_0 \frac{\sin(k_x x_0)}{k_x} \frac{\sin(k_y y_0)}{k_y}. \end{aligned} \quad (36)$$

Otherwise there would be an extra force pulling all particles towards the center of the sheet.

We have discussed in the introduction that the reason for the success of the infinite shearing sheet model describing spiral density waves realistically is the rapid convergence of the Poisson integral in self gravitating disks and that the “effective range” of gravity of the density waves is only of the order  $\lambda_{\text{crit}}/2$ . Thus, if the size of the simulated sheet is chosen large enough, it should behave like an infinite shearing sheet. Next the wave numbers are discretized with bin widths  $\Delta k_x$  and  $\Delta k_y$ , respectively. Discretizing equations (33) accordingly we obtain for the planar components of the gradient of the gravitational potential

$$\begin{aligned} -\nabla\Phi(\mathbf{R}_j, z=0) &= \sum_{\mathbf{k}_{x,n}} \Delta k_x \sum_{\mathbf{k}_{y,n}} \Delta k_y \frac{G\mathbf{k}_n}{\pi \sqrt{k_{x,n}^2 + k_{y,n}^2}} \\ &\times [-A(\mathbf{k}_n) \sin(\mathbf{k}_n, \mathbf{R}_j) + B(\mathbf{k}_n) \cos(\mathbf{k}_n, \mathbf{R}_j)], \end{aligned} \quad (37)$$

with  $\mathbf{k}_n = (k_{x,n}, k_{y,n})$ . In each time step of the numerical algorithm the coefficients  $A(\mathbf{k}_n)$  and  $B(\mathbf{k}_n)$  and the forces

(37) due to the fluctuations in the sheet are calculated anew. Then all particles are moved one time step ahead. The equations of motion are the epicyclic equations of motion augmented by the fluctuating forces (Toomre 1981, 1990),

$$\begin{aligned} \ddot{x} &= 2\Omega_0 \dot{y} + 4\Omega_0 A - \frac{\partial\Phi}{\partial x}(x, y), \quad u = \dot{x}, \\ \ddot{y} &= -2\Omega_0 \dot{x} - \frac{\partial\Phi}{\partial y}(x, y), \quad v = \dot{y} + 2Ax. \end{aligned} \quad (38)$$

In a quiet disk the fluctuating forces would be zero and the particles would follow simply epicyclic orbits. In the simulations the equations of motion (38) are integrated numerically using the symplectic integrator described in the appendix.

### 3.2. Trial runs

The basic dynamics of the shearing sheet is characterized by Oort’s constants  $A = -\frac{1}{2}R_0 \frac{d\Omega_0}{dR_0}$ ,  $B = A - \Omega_0$ , the epicyclic frequency of the particle orbits  $\kappa = \sqrt{-4\Omega_0 B}$ , the epicyclic ratio of the velocity dispersions of the particles  $\sigma_u^2/\sigma_v^2 = 4\Omega_0^2/\kappa^2$ , the critical wave number  $k_{\text{crit}} = \kappa^2/(2\pi G\Sigma_0)$  and the critical wave length  $\lambda_{\text{crit}} = 2\pi/k_{\text{crit}}$ , and finally the Toomre stability parameter  $Q = \kappa\sigma_u/(3.36G\Sigma_0)$ . We introduce dimensionless model units in the following way. The length unit is  $\lambda_{\text{crit}} = 1$  and accordingly the wave number unit  $k_{\text{crit}} = 2\pi$ . We set  $G\Sigma_0 = 1$  which implies  $\kappa = 2\pi$ . The time unit is then the epicyclic period  $t_\kappa = 1$ . Moreover we assume a flat rotation curve,  $A = -B = \frac{1}{2}\Omega_0$  so that  $A = -B = \frac{\pi}{\sqrt{2}}$  and  $\Omega_0 = \sqrt{2}\pi$ . The radial velocity dispersion is given by  $\sigma_u = \frac{3.36}{2\pi}Q$  and the epicyclic ratio is  $\sigma_u/\sigma_v = \sqrt{2}$ . In all the simulations presented here we have used the following parameters:

number of particles  $N = 32768$

size  $x_0=10$ ,  $y_0 = \sqrt{2}x_0 = 14.1$

time step 0.03125

bin size of wave numbers  $\Delta k_x = \Delta k_y = 0.0625$

64 bins in  $k_x$  ranging from -4 to 4

32 bins in  $k_y$  ranging from 0 to 4

$Q=1.2$

The simulations were set up as illustrated in Fig. 2 according to Sellwood’s (1983) quiet start recipe where the particles are distributed spatially homogeneously and according to a Schwarzschild distribution in velocity space. In Fig. 3 we show the simulation of the dynamical evolution of the shearing sheet over 4 time units as snapshots of the 32768 particle positions. The sheet, which was initially homogeneous, quickly develops density waves which can be seen as streaks in the frames in Fig. 3 in the time interval  $t \approx 1$  to 2. However, the sheet then becomes featureless again. This is due to rapid dynamical heating of the sheet which was already observed by Sellwood & Carlberg (1984) and in other numerical simulations of the dynamical evolution of galactic disks such as by Tomley

**Fig. 3.** Dynamical evolution of the shearing sheet. Snapshots of particle positions are shown for  $t = 0.5, 1, \dots 3.5$ , and 4, respectively. The  $y$ -axis is oriented in the direction of the shear flow. The size of each frame is the same as in Fig. 2

**Fig. 5.** Same as Fig. 3, but the shearing sheet is dynamically cooled by accretion of particles during the simulation.

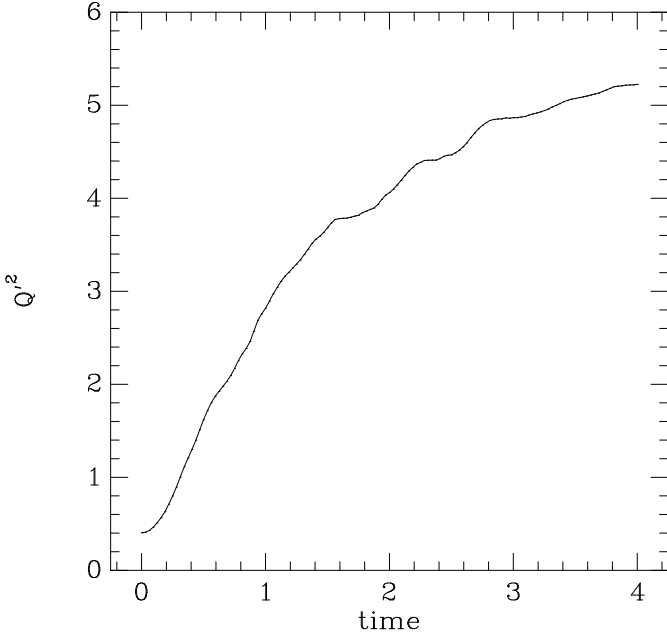


**Fig. 4.** The rise of  $Q'^2 = \langle u^2 \rangle / \Sigma_0^2$  as function of time illustrating the disk heating. The time unit is the epicyclic period.

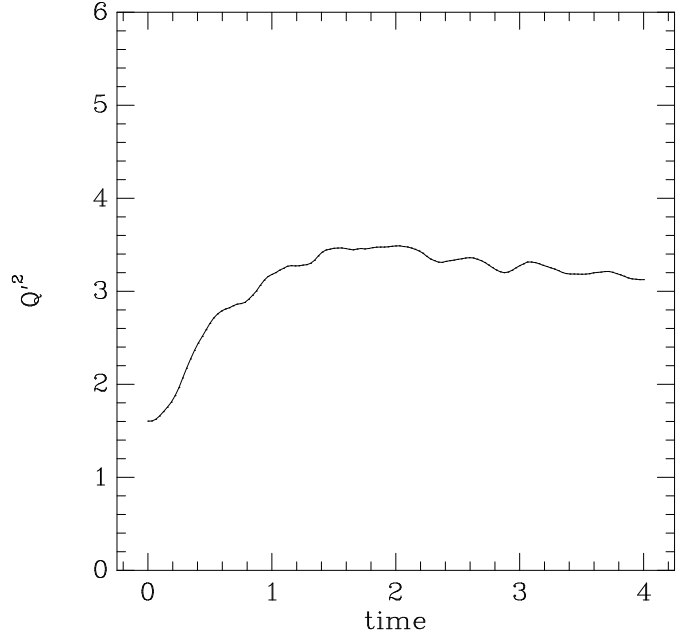


**Fig. 6.** Same as Fig. 4, but the shearing sheet is dynamically cooled by accretion of particles during the simulation.

et al. (1991), Toomre (1990), Toomre & Kalnajs (1991), Chiueh & Tseng (2000). We illustrate the dynamical heating in Fig. 4 where we show the evolution of the ratio  $Q'^2 = \langle u^2 \rangle / \Sigma_0^2$ , which mimics the  $Q$  parameter, as function of time. During the evolution of the sheet its value has risen from 0.4 to 5.2, which reflects the rise of the velocity dispersion of the particles with time and that the sheet has become dynamically hot. The nearly linear rise of  $Q'^2$  in the early phases of the simulation nicely fits the dynamical disk heating effect of density waves described theoretically by Fuchs (2001b) and Griv et al. (2002). In order to remedy this effect we have cooled the sheet dynamically like Sellwood & Carlberg (1984) by adding during the simulation particles on orbits with their initial epicycle amplitudes. In Figs. 5 and 6 we show the results of a simulation which grew linearly from 16384 particles to 32768 particles as in the previous simulation. As can be seen from Figs. 5 and 6 the density wave activity and the pseudo- $Q$  parameter stayed fairly constant throughout the simulation, even though the velocity dispersion of the particles was rising. Since the  $Q'$  parameter is larger than in the initial stages of the previous run, the amplitudes of the density waves shown in Fig. 5 are smaller than in the early frames of Fig. 3. We illustrate the tips of the spiked amplitude distribution of the  $A(\mathbf{k})$  Fourier coefficients of the density waves in Fig. 7. The distribu-

tion of the  $B(\mathbf{k})$  Fourier coefficients is very similar. As expected from linear theory (Julian & Toomre 1965, Toomre 1981, Fuchs 2001a) density waves with wave numbers in the region around  $\mathbf{k} \approx (1, 0.5) k_{\text{crit}}$  implying pitch angles of about  $27^\circ$  have the largest amplitudes. These are the streaks seen in Fig. 5. They are, however, not stationary patterns, but formed by the superposition of transient shearing density waves. A cut through the power spectrum  $\sqrt{A^2(\mathbf{k}) + B^2(\mathbf{k})}$  of the density wave amplitudes at a given  $k_y$  wave number is also instructive. In Fig. 8 cuts at  $k_y = 0.5 k_{\text{crit}}$  are illustrated for the initial ( $t = 0$ ) and a later stage ( $t = 2$ ) of the simulation. Initially the power spectrum is flat in accordance with random distribution of the disk particles. Later on the power spectrum develops not only the high peak at positive  $k_x \approx 1 k_{\text{crit}}$  wave numbers which corresponds to the maximally swing amplified amplitudes of the shearing density waves, but is also significantly higher at negative  $k_x$  wave numbers than the power spectrum of randomly distributed particles. Such leading density waves are the input to the swing amplification mechanism. We conclude in agreement with Sellwood & Carlberg (1984), who presented a similar argument, that the recurring density waves are indeed not amplified random noise, but are connected events. The enhanced power at leading wave numbers supports the argument that the coupling of trailing density waves can lead to leading input to the swing amplifier.



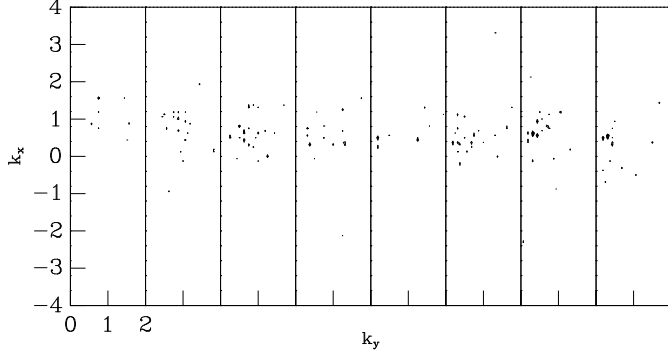


**Fig. 7.** Peaks of positive  $A(\mathbf{k})$  Fourier coefficients in the simulations presented in Fig. 5 at times  $t = 0.5, 1, \dots, 3.5$ , and 4, respectively. For clarity only contour levels of at least 40% of the maxima of the spikes are shown. The wave numbers are given in units of  $k_{\text{crit}}$ .

The SCF simulations shown in Fig. 5 look very similar to the direct N-body simulations of the dynamical evolution of the shearing sheet by Toomre (1990) and Toomre & Kalnajs (1991). In these simulations an artificial friction force acting on the particles in the sheet is included in order to overcome the disk heating problem. Toomre & Kalnajs (1991) explain the ‘hotch-potch of swirling density waves’ as the collective response of the shearing sheet to each of its individual members by polarization clouds around each particle. Instead of this quasi-linear concept we prefer to interpret our simulations in terms of the feedback cycle described in section (2). The SCF simulations illustrated in Fig. 5 resemble closely the direct N-body simulations of Chiueh & Tseng (2000, their run a). Disk heating effects are apparently controlled there by the choice the softening length.

### 3.3. Exciting a swing amplified density wave

The numerically simulated shearing sheet is subjected to a “strong” external potential perturbation of the form considered in section (2.5),

$$\delta\Phi_{\mathbf{k}} \propto \delta(k_x - (k_x^{\text{in}} + 2Ak_y t))\delta(k_y - k_y^{\text{in}})e^{-\frac{t^2}{T^2}}. \quad (39)$$

It was shown in paper (I) that according to linear theory the shearing sheet responds with a swing amplified shearing density wave. In Fig. 9 the result of a simulation with a time constant of  $T = 1.8$  is traced in  $\mathbf{k}$ -wave-vector space. As can be seen from Fig. 9 the disk response is indeed of exactly the same nature as predicted by linear theory. The impulse travels from negative  $k_x$  to positive wave numbers and the amplitude is maximally amplified around  $k_x \approx 2$ .

### 3.4. Non-linear wave coupling

The shearing sheet is now subjected to two independent impulsive external potential perturbations of the form given in equation (39) with initial wave vectors  $\mathbf{k}^{\text{in},1}$  and  $\mathbf{k}^{\text{in},2}$ , respectively. As shown in Figs. 10 and 11 both per-

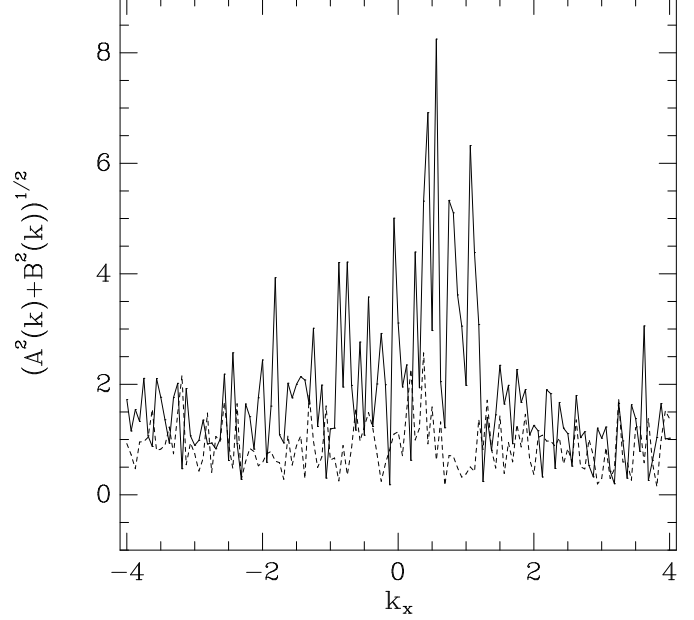


**Fig. 8.** Power spectrum  $\sqrt{A^2(k_x, 0.5) + B^2(k_x, 0.5)}$  of the density wave amplitudes in the simulation shown in Fig. 5. The dashed and solid lines correspond to times  $t = 0$  and  $t = 2$ , respectively. The wave numbers are given in units of  $k_{\text{crit}}$ .

turbations evolve like the single perturbation in the previous section. However, further density waves appear with circumferential wave numbers  $k_y$  as predicted by the sum rule given in equation (19). We interpret these new density waves, which are delayed relative to the imposed perturbations, as examples of the onset of the non-linear feedback cycle predicted theoretically in section (2). In Fig. 10 an example is shown which started with the initial wave vectors  $\mathbf{k}^{\text{in},1} = (-2, 0.5)k_{\text{crit}}$  and  $\mathbf{k}^{\text{in},2} = (-3, 1)k_{\text{crit}}$ , respectively. At time  $t=0.88$  there appears a new weak feature at about  $\mathbf{k} = (0.9, 1.5)k_{\text{crit}}$ . This then couples back with the first externally triggered wave leading to a strong wave at time  $t = 1.13$  with  $k_y = 1k_{\text{crit}}$ , which travels behind the second externally triggered wave. The example in Fig. 11 started with initial wave vectors  $\mathbf{k}^{\text{in},1} = (-2, 0.5)k_{\text{crit}}$  and  $\mathbf{k}^{\text{in},2} = (-3, 1.5)k_{\text{crit}}$ , respectively. At time  $t=0.5$  a new weak feature appears at about  $\mathbf{k} = (-3, 1.5)k_{\text{crit}}$ . After the second externally triggered wave was wrapped up very tightly, so that it travelled out of the frames shown in Fig. 11, there appears at time  $t = 1.13$  a new strong wave at  $\mathbf{k} = (1, 1)k_{\text{crit}}$ . Non-linear coupling of density waves with different wave numbers, which led to recurrent density wave activity, has already been noted by Chiueh & Tseng (2000) in their simulations, although no detailed explanation was offered. They also find the decline of the amplitudes of density waves at given  $k_y$  wave number which they ascribe to Landau damping. However, since density waves in the shearing sheet swing around with the shear flow, there is effectively no relative streaming of disk particles relative to the waves (cf. Fig. 3 of Toomre 1981), which would lead to Landau damping (Lynden-Bell & Kalnajs

**Fig. 9.** Response of the shearing sheet to an external impulsive potential perturbation with an initial wave vector  $(k_x, k_y) = (-2, 0.5) k_{\text{crit}}$  traced in wave number space. Frames are shown for time  $t = 0, 0.25, \dots, 1.5$ , and  $1.75$ , respectively.

**Fig. 10.** Response of the shearing sheet to two external impulsive potential perturbations with initial wave vectors  $(k_x, k_y) = (-2, 0.5) k_{\text{crit}}$  and  $(k_x, k_y) = (-3, 1) k_{\text{crit}}$ , respectively traced in wave number space. Frames are shown for time  $t = 0, 0.25, 0.5, 0.88, 1.0, 1.13, 1.25$ , and  $1.38$ , respectively.

**Fig. 11.** Same as Fig. 8, but with two external impulsive potential perturbations with initial wave vectors  $(k_x, k_y) = (-2, 0.5) k_{\text{crit}}$  and  $(k_x, k_y) = (-3, 1.5) k_{\text{crit}}$ , respectively. Frames are shown for time  $t = 0, 0.25, 0.5, 0.75, 1.0, 1.13, 1.25$ , and  $1.38$ , respectively.

1972). Thus in our view hardly any Landau damping is to be expected. The density waves die out, because the density contrast is wiped out by the epicyclic motions of the stars, when the density wave crests are wrapped up tightly by the shear (Julian & Toomre 1966, Fuchs 2001a).

#### 4. Summary and conclusion

The aim of this paper is to study non-linear effects in the dynamical evolution of an unbounded shearing sheet made of stars, which models a patch of a galactic disk. We have analyzed these effects both theoretically and by numerical simulations.

First we have investigated theoretically the implication of the non-linear term of the Boltzmann equation for the dynamical evolution of the shearing sheet. The non-linear term is expressed in terms of Fourier expansions of the perturbations of the distribution function of the stars in phase space and the gravitational potential of the sheet, respectively, and the Boltzmann equation augmented by this term is formally solved. It is shown that this further term can be viewed formally as an inhomogeneity of the fundamental Volterra integral equation which describes the dynamical evolution of the shearing sheet. The inhomogeneity is given by combinations of the Fourier coefficients of the perturbations of the distribution function and the gravitational potential of the sheet, sampled over the past history of the evolution of the sheet. This leads to a feedback cycle for swing amplified density waves. It is quite different from the effect of non-linearities of the hydrodynamical or Jeans equations, which have been used alternatively to describe the dynamics of the shearing sheet or galactic disks.

In order to present concrete examples of the non-linear feedback cycle we have developed a self-consistent field code and have run numerical simulations of the dynamical evolution of the shearing sheet. The SCF method is based on a set of pairwise basis functions into which the surface density and the gravitational potential of the shearing sheet are expanded. Each of the pairwise basis functions solve the Poisson equation. In the case of the shearing sheet these are simply Fourier transforms. The equations of motion of the particles in the shearing sheet are the epicyclic equations of motion, which describe the motion

of the particles in the unperturbed sheet, augmented by the forces due to the fluctuations of the sheet. In the simulations the shearing sheet turned out to be prone to rapid dynamical heating. Thus it was necessary to cool the sheet dynamically by adding mass continuously to the sheet during the simulations. We have shown that the live shearing sheet responds to impulsive external potential perturbations by developing shearing density waves. In particular, by applying simultaneous multiple perturbations we have demonstrated the appearance of non-linearly induced shearing density waves, exactly as theoretically predicted.

The feedback cycle found here might well account for the hitherto unexplained recurrent shearing spiral instabilities seen in the large scale numerical simulations of the dynamical evolution of galactic disks.

*Acknowledgements.* We are indebted to the anonymous referee for comments that helped to improve the paper. B.F. thanks E. Sedlmayr and H. Völk for their encouragement to pursue non-linear studies. T.T. acknowledges support by a grant from the Alexander-von-Humboldt foundation.

#### References

- Chiueh, T., Tseng, Y.H., 2000, ApJ 544, 204
- Fuchs, B., 1991, in: B. Sundelius (ed.) Dynamics of Disc Galaxies, CTH Göteborg, p. 359
- Fuchs, B., 2001a, A&A 368, 107 (paper I)
- Fuchs, B., 2001b, MNRAS 325, 1637 (paper III)
- Fuchs, B., 2004, A&A 419, 941 (paper IV)
- Fuchs, B., 2005, A&A submitted (paper II)
- Fuchs, B., von Linden, S., 1998, MNRAS 294, 513
- Goldreich, P., Lynden-Bell, D., 1965, MNRAS 130, 125
- Griv, E., Gedalin, M., Yuan, C., 2002, A&A 383, 338
- Hockney, R. W., Eastwood, J. W., 1988, Computer simulation using particles, Hilger, Bristol
- Ikeuchi, S., Nakamura, T., 1976, Prog. Theoret. Phys. 55, 1419
- Julian, W.H., Toomre, A., 1966, ApJ 146, 810
- Kalnajs, A.J., 1971, ApJ 166, 275
- Lynden-Bell, D., Kalnajs, A., 1972, MNRAS 157, 1
- Meinel, R., 1983, AN 304, 65
- Norman, C.A., 1978, MNRAS 182, 457
- Sellwood, J.A., 1983, JCoPh 50, 337
- Sellwood, J.A., 1989, in: J.A. Sellwood (ed.) Dynamics of Astrophysical Discs, Cambridge Univ. Press, Cambridge, p. 155

Sellwood, J.A., 2000, ASS 272, 31  
 Sellwood, J.A., Carlberg, R.G., 1984, ApJ 282, 61  
 Sellwood, J.A., Kahn, F.D., 1991, MNRAS 250, 278  
 Sellwood, J.A., Lin, D.N.C., 1989, MNRAS 240, 991  
 Sygnet, J.F., Tagger, M., Athanassoula, E., Pellat, R., 1988, MNRAS 232, 733  
 Tomley, L., Cassen, P., Steiman-Cameron, T., 1991, ApJ 382, 530  
 Tagger, M., Sygnet, J.F., Athanassoula, E., Pellat, R., 1987, ApJ 318, L43  
 Toomre, A., 1981, in: S.M. Fall, D. Lynden-Bell (eds.) The Structure and Evolution of Normal Galaxies, Cambridge Univ. Press, Cambridge, p. 111  
 Toomre, A., 1990, in: R. Wielen (ed.) Dynamics and Interactions of Galaxies, Springer, Berlin, p. 292  
 Toomre, A., Kalnajs, A.G., 1991, in: B. Sundelius (ed.) Dynamics of Disc Galaxies, CTH Göteborg, p. 341  
 Wisdom, J., Tremaine, S., 1988, AJ 95, 925

## Appendix A: A generalized leap-frog scheme

We consider a set of ordinary differential equations

$$\dot{u} = f(u, x), \quad \dot{x} = g(u, x), \quad (\text{A.1})$$

where  $u$  and  $x$  may be also vectors. Integrating equations (A.1) by a small time step  $h$  from  $t_0$  to  $t_0 + h$  leads to

$$\begin{aligned} u(t_0 + h) &= u_0 + \dot{u}_0 h + \frac{1}{2} \ddot{u}_0 h^2 + O(h^3) \\ &= u_0 + f(u, x)h + \frac{1}{2} \dot{f}(u, x)h^2 + O(h^3) \\ &= u_0 + f(u, x)h + \frac{1}{2} h^2 \left[ \left( f \cdot \frac{\partial}{\partial u} \right) f + \left( g \cdot \frac{\partial}{\partial x} \right) f \right] \\ &\quad + O(h^3), \\ x(t_0 + h) &= x_0 + \dot{x}_0 h + \frac{1}{2} \ddot{x}_0 h^2 + O(h^3) \\ &= x_0 + g(u, x)h + \frac{1}{2} \dot{g}(u, x)h^2 + O(h^3) \\ &= x_0 + g(u, x)h + \frac{1}{2} h^2 \left[ \left( f \cdot \frac{\partial}{\partial u} \right) g + \left( g \cdot \frac{\partial}{\partial x} \right) g \right] \\ &\quad + O(h^3). \end{aligned} \quad (\text{A.2})$$

Adopting the principle of the leap-frog algorithm (Hockney & Eastwood 1988) we introduce *mid-points*,

$$x_{1/2} = x(t_0 + h/2), \quad u_{1/2} = u(t_0 + h/2), \quad (\text{A.4})$$

and can write

$$\begin{aligned} f(u_0, x_{1/2}) &= f(u_0, x_0) + \frac{h}{2} \left( g(u_0, x_0) \cdot \frac{\partial}{\partial x} \right) f + O(h^2), \\ g(u_{1/2}, x_0) &= g(u_0, x_0) + \frac{h}{2} \left( f(u_0, x_0) \cdot \frac{\partial}{\partial u} \right) g + O(h^2). \end{aligned} \quad (\text{A.5})$$

It follows then

$$\begin{aligned} u(t_0 + h) &= u_0 + hf(u_0, x_{1/2}) \\ &\quad + \frac{h^2}{2} \left( f(u_0, x_0) \cdot \frac{\partial}{\partial u} \right) f(u_0, x_0) + O(h^3) \\ &= u_0 + hf(u_0, x_{1/2}) \\ &\quad + \frac{h^2}{2} \left( f(u_0, x_{1/2}) \cdot \frac{\partial}{\partial u} \right) f(u_0, x_{1/2}) + O(h^3), \\ x(t_0 + h) &= x_0 + hg(u_{1/2}, x_0) \end{aligned}$$

$$\begin{aligned} &+ \frac{h^2}{2} \left( g(u_0, x_0) \cdot \frac{\partial}{\partial x} \right) g(u_0, x_0) + O(h^3) \\ &= x_0 + hg(u_{1/2}, x_0) \\ &+ \frac{h^2}{2} \left( g(u_{1/2}, x_0) \cdot \frac{\partial}{\partial x} \right) g(u_{1/2}, x_0) + O(h^3), \end{aligned} \quad (\text{A.6})$$

and finally

$$\begin{aligned} u_{1/2} &= u_{-1/2} + hf(u_{-1/2}, x_0) \\ &+ \frac{h^2}{2} \left( f(u_{-1/2}, x_0) \cdot \frac{\partial}{\partial u} \right) f(u_{-1/2}, x_0) + O(h^3) \\ x_1 &= x_0 + hg(u_{1/2}, x_0) \\ &+ \frac{h^2}{2} \left( g(u_{1/2}, x_0) \cdot \frac{\partial}{\partial x} \right) g(u_{1/2}, x_0) + O(h^3). \end{aligned} \quad (\text{A.7})$$

The equations of motion (36) of the particles in the shearing sheet can be written as a set of first order differential equations,

$$\begin{aligned} \dot{u} &= 2\Omega_0 v + f_x \\ \dot{v} &= 2Bu + f_y \\ \dot{x} &= u \\ \dot{y} &= v - 2Ax. \end{aligned} \quad (\text{A.8})$$

From equations (A.7) we derive the leap-frog scheme

$$\begin{aligned} u_{1/2} &= u_{-1/2} + h \left[ 2\Omega_0 v_{-1/2} + f_x(x_0, y_0) \right] \\ &+ h^2 \Omega_0 \left[ 2Bu_{-1/2} + f_y(x_0, y_0) \right] + O(h^3), \\ v_{1/2} &= v_{-1/2} + h \left[ 2Bu_{-1/2} + f_y(x_0, y_0) \right] \\ &+ h^2 (A - \Omega_0) \left[ 2\Omega_0 v_{-1/2} + f_x(x_0, y_0) \right] + O(h^3), \\ x_1 &= x_0 + hu_{1/2} + O(h^3) \\ y_1 &= y_0 + h(v_{1/2} - 2Ax_0) - h^2 Au_{1/2} + O(h^3). \end{aligned} \quad (\text{A.9})$$

The time step was set to  $h = 0.03125$  in the simulations. Thus the orbits are integrated with an accuracy of  $h^2 = 0.001$ .

This figure "2657fig2.jpg" is available in "jpg" format from:

<http://arxiv.org/ps/astro-ph/0508393v1>

This figure "2657fig3.jpg" is available in "jpg" format from:

<http://arxiv.org/ps/astro-ph/0508393v1>

This figure "2657fig5.jpg" is available in "jpg" format from:

<http://arxiv.org/ps/astro-ph/0508393v1>

This figure "2657fig9.jpg" is available in "jpg" format from:

<http://arxiv.org/ps/astro-ph/0508393v1>

This figure "2657fi10.jpg" is available in "jpg" format from:

<http://arxiv.org/ps/astro-ph/0508393v1>



This figure "2657fi11.jpg" is available in "jpg" format from:

<http://arxiv.org/ps/astro-ph/0508393v1>